Characterization of a Two-Dimensional Subsurface Object With an Effective Scattering Model

Neil V. Budko and Peter M. van den Berg

***Abstract*—The problem of the location and characterization of a two-dimensional (2-D) subsurface object is formulated as the inverse problem for an effective scattering model. An arbitrary finite-sized buried object is described as a subsurface circular cylinder with the radius, permittivity, and position of its center to be determined. The inversion is performed in a nonlinearized way, minimizing the discrepancy between the actual scattered field and that of the effective scattering model. A simple and quick solution for a circular cylinder embedded in a lossy half space is introduced. As far as numerical efficiency is concerned, the obtained approximate algorithm is comparable to the free-space solution. The location algorithm has been tested with the two-dimensional models of plastic antipersonnel land mines.**

***Index Terms*— Detection and characterization of subsurface objects, ground penetrating radar, nonlinear inversion.**

I. Introduction

IN this paper, we consider the problem of an effective parametric characterization of a two-dimensional subsurface object from a limited set of measured scattered electromagnetic field data. Most of the solutions to the inverse problem of subsurface scattering configurations are known to be sensitive to the initial estimate of the location, size, and constitutive parameters of the buried object, especially in the case of the ground penetrating radar (GPR) bistatic measurement setup, which normally does not provide a complete and accurate measurement of the scattered field's spatial distribution. Another important question addressed in this work is the practical real-time applicability of the algorithm. Such an algorithm must be fast enough to be useful in land mine detection, for example.

Our preliminary studies were concerned with the free-space scattering configuration [1], where we had developed an effective forward and inverse scattering model, based on the concept of an approximate T-matrix. Actually, an arbitrary finite-sized object was described with the help of the effective homogeneous circular scatterer, restoring its location, radius, and permittivity in the process of nonlinear minimization of the discrepancy between the field scattered by the unknown object and the field scattered by the effective circular substitute. With this, the necessary initial estimate of the effective parameters of the real object (position, size, and constitution) were obtained, which are also useful for the immediate preliminary characterization.

In the present paper, the unknown object is supposed to be located in a lossy half space. We show how the structure of the background media can be taken into account within concepts of the T-matrix approach, so that previously developed results of the approximate T-matrix are easily extended to the present case. We use a slightly modified version of the conventional T-matrix approach [2], which follows the ideas mentioned in [3] and realized in [4].

The solution to the forward scattering problem for the two-media configuration employs the Green function in the form of an inverse Fourier transform. This complicates the procedure, developing a forward scattering code and particularly an inverse scattering code, both of which would be applicable in the real time, since calculation of the Green function includes repetitious adaptive integration in complex domain [6], [7]. The first part of this paper is devoted to the analysis and the effective approximation of the two-media Green function. As a result, we obtain expressions that are equivalent to those for the free-space configuration as far as numerical efficiency is concerned. Also, we make a numerical comparison of our approximation with the one most frequently used in the literature, viz., the one where the Green function of the two-media background simply is replaced by the Green function of an infinite homogeneous medium with the material parameters of the lower half space. This latter approximation appears to be too crude. Finally, some numerical experiments with the inversion algorithm are discussed.

II. Scattering Configuration

In a two-dimensional (2-D) case, we consider an inhomogeneous object, with its axis along the y-direction of a Cartesian coordinate system, immersed in a background that consists of two half spaces with a plane interface at $z = 0$. The permittivity ε_0 and the electrical conductivity σ_0 are the constitutive parameters of the upper half space $z < 0$, while the lower one $z > 0$ is characterized by the permittivity ε_1 and conductivity σ_1. Fig. 1 shows the cross section of the configuration in the (x, z)-plane. The dielectric material inside the cylinder is characterized by the permittivity $\varepsilon(\mathbf{r})$ and the conductivity $\sigma(\mathbf{r})$, $\mathbf{r} = (x, z)$. The measurement setup, which is widely used in GPR applications, is considered the bistatic model with the fixed source-receiver offset R_0. We assume that the object is illuminated by a TM-polarized wave ($\mathbf{E}$ is parallel to the cylinder axis) generated by a single line source. Scattered data are collected in the process of the movement of the source-receiver unit along a horizontal section of length R_a. We assume that the transient scattered data are transformed

Manuscript received September 8, 1998; revised January 28, 1999. This work was supported in part by FEL TNO, The Netherlands.

The authors are with the Laboratory of Electromagnetic Research, IRCTR, Delft University of Technology, 2600 GA Delft, The Netherlands.

Publisher Item Identifier S 0196-2892(99)06270-1.

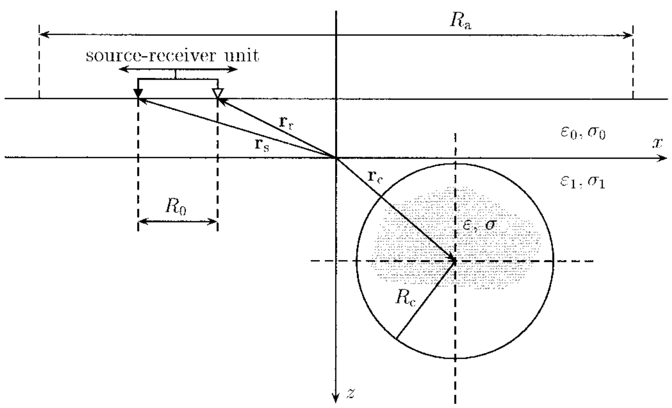

Fig. 1. Scattering configuration.

to the frequency domain, and the analysis will be in this frequency domain with time factor $\exp(-i\omega t)$.

III. Green's State of the Background Medium

The fundamental difference between scattering from free-space and subsurface objects stems from the presence of the plane interface in the latter case. We treat the problem by employing the concept of background medium, which requires a rigorous analysis of its Green state. This Green's state $G(\mathbf{r}, \mathbf{r}')$ is the field at a point $\mathbf{r}$ due to a line source at $\mathbf{r}'$ in the background medium.

A. Expanded Form of the Green Function and the T-Matrix Relation

Suppose the Green function of the background medium is obtainable in a form of expansion as

$$G(\mathbf{r}, \mathbf{r}') = \sum_m \Psi_m(\mathbf{r}')\Psi_m^{\text{reg}}(\mathbf{r}). \tag{1}$$

The functions $\Psi_m(\mathbf{r}')$ are singular but satisfy the radiation conditions for $|\mathbf{r}'| \to \infty$, while the functions $\Psi_m^{\text{reg}}(\mathbf{r})$ are regular. The incident field in the background medium is the field in absence of the scattering object and may be written as

$$u^{\text{inc}}(\mathbf{r}) = G(\mathbf{r}, \mathbf{r}_s) \tag{2}$$

where $\mathbf{r}_s$ is the source point of the transmitter. Substitution of the Green function in its expanded form (1) into (2) yields

$$u^{\text{inc}}(\mathbf{r}) = \sum_m A_m(\mathbf{r}_s)\Psi_m^{\text{reg}}(\mathbf{r}) \tag{3}$$

with

$$A_m(\mathbf{r}_s) = \Psi_m(\mathbf{r}_s). \tag{4}$$

From the contrast source or other formulation, one can recall that the relation between the scattered field and the Green function of the background is a linear integral representation. In operator form, we write

$$u^{\text{sct}}(\mathbf{r}_r) = LG \tag{5}$$

where $\mathbf{r}_r$ denotes the receiver point. Substituting the Green function here in its expanded form (1), we obtain

$$u^{\text{sct}}(\mathbf{r}_r) = \sum_m B_m \Psi_m(\mathbf{r}_r) \tag{6}$$

with the unknown quantity

$$B_m = L\Psi_m^{\text{reg}}. \tag{7}$$

From the linearity of both the initial and scattered fields (with respect to the Green function), it is clear that a linear relation exists between the quantities A_m and B_m. This relation may be written down with the help of the T-matrix as

$$B_m = \sum_{m'} T_{mm'} A_{m'}. \tag{8}$$

The T-matrix contains the description of a particular scatterer. In addition, the process of its calculation implements a particular method to solve the direct scattering problem. The above formulation shows that as soon as the Green function of the background medium is written in the expanded form (1), both the initial and scattered fields may be represented with the help of the expansion functions $\Psi_m(\mathbf{r})$ and $\Psi_m^{\text{reg}}(\mathbf{r})$ [see (3) and (6)], and a linear T-matrix relation (8) between the expansion coefficients of initial and scattered fields may be established. The completeness of the systems of functions $\{\Psi\}$ and $\{\Psi^{\text{reg}}\}$ versus their actual shape has been studied in detail elsewhere (see [5] and references therein).

B. Exact Expanded Form of the Green Function

In the 2-D case, the Green function of a homogeneous medium with wavenumber $k_1 = \omega\sqrt{\varepsilon_1\mu + i\sigma_1\mu/\omega}$ may be written in the integral form as

$$G_1(\mathbf{r}, \mathbf{r}') = \frac{i}{4\pi}\int_{-\infty}^{\infty} \frac{1}{\gamma_1} e^{i\alpha(x-x') + i\gamma_1|z-z'|}\, d\alpha \tag{9}$$

where $\gamma_1 = \sqrt{k_1^2 - \alpha^2}$ is the propagation coefficient or in the equivalent form through the Hankel function as

$$G_1(\mathbf{r}, \mathbf{r}') = \frac{i}{4} H_0^{(1)}(k_1|\mathbf{r}' - \mathbf{r}|). \tag{10}$$

Employing the addition theorem for cylindrical functions, the Green function is obtained in the expanded form as

$$G_1(\mathbf{r}, \mathbf{r}') = \frac{i}{4}\sum_{m=-\infty}^{\infty} H_m^{(1)}(k_1|\mathbf{r}' - \mathbf{r}_c|) J_m(k_1|\mathbf{r} - \mathbf{r}_c|) \times e^{im(\theta' - \theta)} \tag{11}$$

when $|\mathbf{r}' - \mathbf{r}_c| \geq |\mathbf{r} - \mathbf{r}_c|$, where $\mathbf{r}_c = \{x_c, z_c\}$ is a reference point in the lower half space and in particular, we later choose $\mathbf{r}_c$ to be the center of the scattering object (see Fig. 1). Furthermore, the angles θ' and θ are defined as

$$\theta' = \text{atan}\left(\frac{z' - z_c}{x' - x_c}\right), \quad \theta = \text{atan}\left(\frac{z - z_c}{x - x_c}\right). \tag{12}$$

Equation (11) provides the necessary representation (1) to use the T-matrix formulation of the problem.

The Green function of the medium, consisting of two half spaces with a plane interface at $z = 0$, has the following integral representation [8]:

$$G_h(\mathbf{r}, \mathbf{r}') = \frac{i}{2\pi} \int_{-\infty}^{\infty} \frac{1}{\gamma_0 + \gamma_1} e^{i\alpha(x-x') + i(\gamma_1 z - \gamma_0 z')} \, d\alpha \quad (13)$$

for $\mathbf{r}$ and $\mathbf{r}'$ belonging to different half spaces (i.e. $z \geq 0$, $z' \leq 0$), and

$$G_h(\mathbf{r}, \mathbf{r}') = G_1(\mathbf{r}, \mathbf{r}') + \frac{i}{4\pi} \int_{-\infty}^{\infty} \frac{\gamma_0 - \gamma_1}{\gamma_1(\gamma_0 + \gamma_1)} \times e^{i\alpha(x-x') + i\gamma_1(z+z')} \, d\alpha \quad (14)$$

for $\mathbf{r}$ and $\mathbf{r}'$ both situated in the lower half space (i.e. $z \geq 0$, $z' \geq 0$). Here, $k_0 = \omega\sqrt{\varepsilon_0 \mu + i\sigma_0 \mu / \omega}$ and $\gamma_0 = \sqrt{k_0^2 - \alpha^2}$ are the wavenumber and propagation coefficient in the upper half space, respectively. The Green function given by (14) consists of two terms, in which the first one is the Green function of the homogeneous medium with the material parameters of the lower half space. The second term takes into account reflection against the plane interface.

To represent the integrals (13), (14) as the series (1), we introduce an alternative form for the employed complex quantities

$$\alpha = k_1 \cos\theta_1, \quad \gamma_1 = k_1 \sin\theta_1 \quad (15)$$

where the complex angle θ_1 follows from

$$e^{i\theta_1} = (\alpha + i\gamma_1)/k_1 = \nu_1. \quad (16)$$

Employing the expansion of the exponential function in terms of Bessel functions

$$e^{ik_1 r\cos(\theta - \theta_1)} = \sum_{m=-\infty}^{\infty} i^m J_m(k_1 r) e^{-im(\theta - \theta_1)} = \sum_{m=-\infty}^{\infty} (i\nu_1)^m J_m(k_1 r) e^{-im\theta} \quad (17)$$

we can expand the integrals (13) and (14) as

$$G_h(\mathbf{r}, \mathbf{r}') = \sum_{m=-\infty}^{\infty} f_m(\mathbf{r}') J_m(k_1|\mathbf{r} - \mathbf{r}_c|) e^{-im\theta} \quad (18)$$

where $f_m(\mathbf{r}')$ is given by

$$f_m(\mathbf{r}') = \frac{i}{2\pi} \int_{-\infty}^{\infty} \frac{(i\nu_1)^m}{\gamma_0 + \gamma_1} e^{i\alpha(x_c - x') + i(\gamma_1 z_c - \gamma_0 z')} \, d\alpha \quad (19)$$

for $\mathbf{r}$ and $\mathbf{r}'$ belonging to different half spaces (i.e. $z \geq 0$, $z' \leq 0$), and

$$f_m(\mathbf{r}') = \frac{i}{4} H_m^{(1)}(k_1|\mathbf{r}' - \mathbf{r}_c|) e^{im\theta'} + \frac{i}{4\pi} \int_{-\infty}^{\infty} \frac{(\gamma_0 - \gamma_1)(i\nu_1)^m}{(\gamma_0 + \gamma_1)\gamma_1} e^{i\alpha(x_c - x') + i\gamma_1(z_c + z')} \, d\alpha \quad (20)$$

for $\mathbf{r}$ and $\mathbf{r}'$ both situated in the lower half space (i.e. $z \geq 0$, $z' \geq 0$).

From the expansions (11) and (18) for the Green functions of free-space and the two-media, we obtain the functions $\Psi_m(\mathbf{r})$ and $\Psi_m^{\text{reg}}(\mathbf{r})$ as

$$\Psi_m(\mathbf{r}') = \frac{i}{4} H_m^{(1)}(k_1|\mathbf{r}' - \mathbf{r}_c|) e^{im\theta'} \quad (21)$$

$$\Psi_m^{\text{reg}}(\mathbf{r}) = J_m(k_1|\mathbf{r} - \mathbf{r}_c|) e^{-im\theta} \quad (22)$$

for a one-medium background, and

$$\Psi_m(\mathbf{r}') = f_m(\mathbf{r}'), \quad (23)$$

$$\Psi_m^{\text{reg}}(\mathbf{r}) = J_m(k_1|\mathbf{r} - \mathbf{r}_c|) e^{-im\theta} \quad (24)$$

for a two-media background. Note that in the latter case, the function $\Psi_m(\mathbf{r})$ has two different representations [(19), (20)] depending upon on the position of $\mathbf{r}$ and $\mathbf{r}'$ with respect to the plane interface.

C. Approximate Expanded Form of the Two-Media Green Function

The exact expanded form of the two-media Green function as introduced in (17) contains the elements $f_m(\mathbf{r})$ given by (19) and (20) that play an important role in the construction of the final solution for the forward scattering problem. Having $f_m(\mathbf{r})$ in the form of complex domain integrals, we would deal with the precise algorithm. This is, however, very slow in a numerical sense. It is natural to consider the possibility of an approximate evaluation of the complex domain integrals involved. First, we note that if we expand the one-medium Green function (9) in the same manner as it was done for the two-media Green function, one arrives at the following integral representation of the Hankel function of the m-th order:

$$\frac{i}{4} H_m^{(1)}(k_1|\mathbf{r} - \mathbf{r}_c|) e^{im\theta} = \frac{i}{4\pi} \int_{-\infty}^{\infty} \frac{1}{\gamma_1} (i\nu_1)^m e^{i\alpha(x_c - x) + i\gamma_1(z_c - z)} \, d\alpha \quad (25)$$

when $z_c \geq z$.

To exploit this relation in (19), we introduce the effective quantities $\gamma_a = \sqrt{k_a^2 - \alpha^2}$, $\nu_a = (\alpha + i\gamma_a)/k_a$ and z_a, and we determine k_a and z_a such that (19) may be approximated by

$$f_m(\mathbf{r}) \approx A \frac{i}{4\pi} \int_0^{\infty} \frac{(i\nu_a)^m}{\gamma_a} e^{i\alpha(x_c - x) + i\gamma_a(z_c - z_a)} \, d\alpha = A \frac{i}{4} H_m^{(1)}(k_a|\mathbf{r}_a - \mathbf{r}_c|) e^{im\theta_a} \quad (26)$$

where A is a suitable damping factor, $\mathbf{r}_a = \{x, z_a\}$, and

$$\theta_a = \operatorname{atan}\left(\frac{\operatorname{Re}(z_a - z_c)}{x - x_c}\right). \quad (27)$$

One can pose a separate algebraic problem for finding the quantities γ_a, k_a, z_a, and ν_a, which allow for the simplification of (26). However, the arising system of equations does not have a closed-form solution for a varying α or for a fixed $\alpha \neq 0$. The simplest available choice is $\alpha = 0$.

Since $\nu_a = \nu_1$ for $\alpha = 0$, one can find k_a and z_a by equalizing the integrands of (26) and (19) at $\alpha = 0$. This leads to the effective wavenumber

$$k_a = (k_0 + k_1)/2 \quad (28)$$

while z_a follows from

$$k_a(z_c - z_a) = k_1 z_c - k_0 z. \tag{29}$$

When k_0 and/or k_1 are complex-valued, a complex-valued result for $z_c - z_a$ is obtained as

$$z_c - z_a = (k_1 z_c - k_0 z)/k_a. \tag{30}$$

The imaginary part of the complex-valued term $z_c - z_a$, which has been omitted in (27), can be incorporated in the damping factor

$$A = e^{-\mathrm{Im}[k_a(z_c - z_a)]}. \tag{31}$$

Now let us turn our attention to the expression (20), which also includes a Fourier integration. Here, we simply approximate the factor $(\gamma_0 - \gamma_1)/(\gamma_0 + \gamma_1)$ by its value at $\alpha = 0$ to obtain

$$f_m(\mathbf{r}) \approx \frac{i}{4} H_m^{(1)}(k_1|\mathbf{r} - \mathbf{r}_c|)e^{im\theta} + \frac{i}{4\pi}\frac{k_0 - k_1}{k_0 + k_1} \times \int_{-\infty}^{\infty} \frac{(i\nu)^m}{\gamma_1} e^{i\alpha(x_c - x) + i\gamma_1(z_c + z)}\, d\alpha. \tag{32}$$

The integral is nothing else than the Hankel function (25) of the image point $\mathbf{r}_i = (x, -z)$. Hence, we obtain

$$f_m(\mathbf{r}) \approx \frac{i}{4} H_m^{(1)}(k_1|\mathbf{r} - \mathbf{r}_c|)e^{im\theta} + \frac{i}{4}\frac{k_0 - k_1}{k_0 + k_1} H_m^{(1)}(k_1|\mathbf{r}_i - \mathbf{r}_c|)e^{im\theta_i} \tag{33}$$

where $\mathbf{r}_i = \{x, -z\}$, while

$$\theta_i = \mathrm{atan}\left(\frac{z_c + z}{x_c - x}\right). \tag{34}$$

The proposed approximation favors the values of the parameter α close to zero. This means that from the whole plane-wave spectrum of the two-media Green function, we select the waves propagating in the directions close to the vertical. It is a remarkable coincidence that the resulting expressions resemble the optical approximation, containing both the transmission and the reflection coefficients. However, in reality, this approximation appears to be more suitable for the low-frequency region, as can be seen from the numerical experiments of the following section.

IV. Effective Circular Scattering Model

The most important feature of the present inversion method is the forthcoming approximation of the T-matrix of the real object by an effective approximation based on the model of a few parameters characterizing the scatterer. Actually, we approximate the T-matrix with the one corresponding to a homogeneous lossy circular cylinder with its center at $\mathbf{r}_c$ and the radius R_c. The parameters that approximately describe the real object are the location $\mathbf{r}_c$ of the center, the radius R_c, the internal permittivity ε_c, and the conductivity σ_c of the homogeneous circular cylinder. This kind of an effective model has appeared to be useful in its free-space counterpart presented earlier in [1].

First, we use the second Green identity to arrive at

$$u^{\mathrm{inc}}(\mathbf{r}) = \int_{\mathbf{r}\in\Gamma} [\partial_n G(\mathbf{r}, \mathbf{r})u(\mathbf{r}) - G(\mathbf{r}, \mathbf{r})\partial_n u(\mathbf{r})]\, ds, \quad \mathbf{r} \in D. \tag{35}$$

Here, D is the cross section of the effective homogeneous cylinder, and Γ is the corresponding boundary with the external normal vector $\mathbf{n}$. To obtain the T-matrix relation, one has to solve the integral equation (35) for the total field $u(\mathbf{r})$ on the boundary Γ. We therefore employ an expansion for the total field and its normal derivative

$$u(\mathbf{r}) = \sum_{m'} C_{m'} \Psi_{m'}^{\mathrm{reg};c}(\mathbf{r}) \tag{36}$$

$$\partial_n u(\mathbf{r}) = \sum_{m'} C_{m'} \partial_n \Psi_{m'}^{\mathrm{reg};c}(\mathbf{r}). \tag{37}$$

Note that in both expansions, we have taken the same expansion coefficients as it was discussed in the null-field literature [2], [3]. The expansion functions $\Psi_m^{\mathrm{reg};c}(\mathbf{r})$ are defined identically to (22), except the wavenumber k_1 is changed to $k_c = \omega\sqrt{\varepsilon_c \mu + i\sigma_c \mu/\omega}$. Using the expanded form (18) of the two-media Green function and the incident field, we obtain the system of linear algebraic equations

$$\sum_{m'} Q_{mm'} C_{m'} = A_m(\mathbf{r}_s) \tag{38}$$

where the Q-matrix is defined as

$$Q_{mm'} = \int_{\mathbf{r}\in\Gamma} \left[\partial_n f_m(\mathbf{r})\Psi_{m'}^{\mathrm{reg};c}(\mathbf{r}) - f_m(\mathbf{r})\partial_n \Psi_{m'}^{\mathrm{reg};c}(\mathbf{r})\right] ds. \tag{39}$$

In this expression, the function f_m is defined either in the exact form by (20) or in the approximate form by (33). In the case of the line source excitation, the expansion coefficients $A_m(\mathbf{r}_s)$ of the incident field are equal to $f_m(\mathbf{r}_s)$, defined either in the exact form by (19) or in the approximate form by (26), while replacing $\mathbf{r}'$ by $\mathbf{r}_s$.

Let us now return to the scattered field at a receiver point $\mathbf{r}_r$ outside D. This scattered field is given by

$$u^{\mathrm{sct}}(\mathbf{r}_r) = \int_{\mathbf{r}\in\Gamma} [G(\mathbf{r}, \mathbf{r}_r)\partial_n u(\mathbf{r}) - \partial_n G(\mathbf{r}, \mathbf{r}_r)u(\mathbf{r})]\, ds, \quad \mathbf{r} \notin D. \tag{40}$$

Using the expanded form (18) of the two-media Green function, the scattered field representation is written as

$$u^{\mathrm{sct}}(\mathbf{r}_r) = \sum_m B_m f_m(\mathbf{r}_r) \tag{41}$$

with the expansion functions f_m defined either in the exact form by (19) or in the approximate form by (26), while the expansion coefficients B_m are obtained as

$$B_m = \sum_{m'} S_{mm'} C_{m'} \tag{42}$$

where the elements of the S-matrix follow from

$$S_{mm'} = \int_{\mathbf{r}\in\Gamma} \left[\Psi_m^{\mathrm{reg}}(\mathbf{r})\partial_n \Psi_{m'}^{\mathrm{reg};c}(\mathbf{r}) - \partial_n \Psi_m^{\mathrm{reg}}(\mathbf{r})\Psi_{m'}^{\mathrm{reg};c}(\mathbf{r})\right] ds. \tag{43}$$

Since the coefficients C_m can be obtained from (38), we rewrite (42) as

$$B_m = \sum_{m'} T_{mm'} A_{m'}(\mathbf{r}_s) \tag{44}$$

with the conventional T-matrix relation

$$T = SQ^{-1}. \tag{45}$$

So far, we have dealt with the general type of cross section of the scattering object D. In case we deal with an effective object of circular shape, we introduce θ as a new integration variable with $ds = R_c\, d\theta$ and R_c as the radius of the circular cylinder. The integrals in the elements of the S-matrix are then carried out analytically with the result

$$\begin{aligned} S_{mm'} = 2\pi R_c[&J_m(R_c k_1)k_c \partial J_{m'}(R_c k_c) \\ &- k_1 \partial J_m(R_c k_1) J_{m'}(R_c k_c)]\delta_{m,-m'} \end{aligned} \tag{46}$$

where ∂J_m denotes the derivative of J_m with respect to its argument, and where $\delta_{m,m'}$ denotes the Kronecker symbol. We observe that even in this half-space problem, the S-matrix remains antidiagonal.

The calculation of Q-matrix is more laborious. The Q-matrix will have the form

$$Q_{mm'} = Q^{(0)}_{mm'} + Q^{(1)}_{mm'} \tag{47}$$

where the first term is determined by the first term (33) with the result that

$$\begin{aligned} Q^{(0)}_{mm'} = \frac{i\pi}{2} R_c\big[&k_1 \partial H^{(1)}_m(R_c k_1) J_{m'}(R_c k_c) \\ &- H^{(1)}_m(R_c k_1) k_c \partial J_{m'}(R_c k_c)\big]\delta_{m,m'} \end{aligned} \tag{48}$$

is a diagonal matrix. The second term of (33) leads to

$$\begin{aligned} Q^{(1)}_{mm'} = &R_c J_{m'}(R_c k_c) \int_0^{2\pi} \partial_{R_c} f^{(1)}_m e^{-im'\theta}\, d\theta \\ &- R_c k_c \partial J_{m'}(R_c k_c) \int_0^{2\pi} f^{(1)}_m e^{-im'\theta}\, d\theta \end{aligned} \tag{49}$$

where $f^{(1)}_m = f^{(1)}_m(R_c, \theta)$ is given either in the exact form

$$\begin{aligned} f^{(1)}_m(R_c, \theta) = \frac{i}{4\pi} \int_{-\infty}^{\infty} &\frac{(\gamma_0 - \gamma_1)(i\nu_1)^m}{(\gamma_0 + \gamma_1)\gamma_1} \\ &\times e^{-i\alpha R_c \cos\theta + i\gamma_1(2z_c + R_c \sin\theta)}\, d\alpha \end{aligned} \tag{50}$$

or in the approximate form

$$f^{(1)}_m(R_c, \theta) \approx \frac{i}{4} \frac{k_0 - k_1}{k_0 + k_1} H^{(1)}_m(k_1 |\mathbf{r}_i - \mathbf{r}_c|) e^{im\theta_i}. \tag{51}$$

One can proceed with further simplifications in the expression (49) by applying the addition theorem to the Hankel function in (51). Relating the image point $\mathbf{r}_i$ to $\mathbf{r}$ (see Fig. 2), we obtain

$$\begin{aligned} &f^{(1)}_m(R_c, \theta) \\ &\quad \approx \frac{i}{4} \frac{k_0 - k_1}{k_0 + k_1} \sum_{n=-\infty}^{\infty} i^{n-m} H^{(1)}_{m+n}(2k_1 z_c) J_n(k_1 R_c) e^{in\theta}. \end{aligned} \tag{52}$$

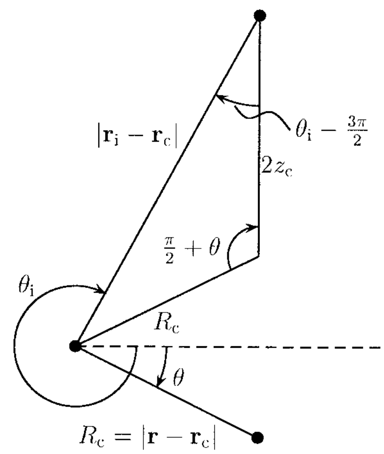

Fig. 2. Relation between $\mathbf{r}_i$ and $\mathbf{r}$.

Using this expression in (49), we obtain an approximate form for $Q^{(1)}_{m,m'}$ as

$$\begin{aligned} Q^{(1)}_{m,m'} \approx \frac{\pi i}{2} \frac{k_0 - k_1}{k_0 + k_1} &R_c i^{(m'-m)} H^{(1)}_{m+m'}(2k_1 z_c) \\ &\times [k_1 \partial J_{m'}(R_c k_1) J_{m'}(R_c k_c) \\ &- J_{m'}(R_c k_1) k_c \partial J_{m'}(R_c k_c)]. \end{aligned} \tag{53}$$

Following the numerical scheme described by the sequence of equations (45), (44), and (41), one can compute the field scattered by a circular cylinder immersed in a lossy half space. If the exact expanded form of the two-media Green function is employed, one deals with the precise forward solution, which includes repetitious evaluation of the complex domain integrals incorporated in the scattered field's expansion functions f_m, in the initial field's expansion coefficients A_m, and in the expansion functions $f^{(1)}_m$ (used in the $Q^{(1)}$ matrix). This makes the inversion algorithm, based on the forward code with the exact Green function, hardly applicable for the real-time data processing.

Employing the approximate expanded form of the two-media Green function, one would deal with the approximate forward code, which does not include Fourier integration at all. Hence, it is simpler and faster from the numerical point of view.

It is worth mentioning that the algorithm can become even simpler without any additional approximations if a particular physical situation is taken into account. For example, at low frequencies and/or in a half space with high electromagnetic losses (e.g., wet soil), one can neglect the mutual scattering between the object and the plane boundary of the half space. For these particular cases, the elements of the $Q^{(1)}$ matrix, which is responsible for the object-interface (multiple) scattering, become negligibly small, so that this matrix does not influence the final result and simply can be omitted.

We conclude this study with a numerical experiment, which is performed to test the validity of the proposed approximate forward scattering model. We also test the applicability of the most frequently used substitute for the two-media Green function, the single-medium Green function (i.e., that of the infinite homogeneous domain with the material parameter of

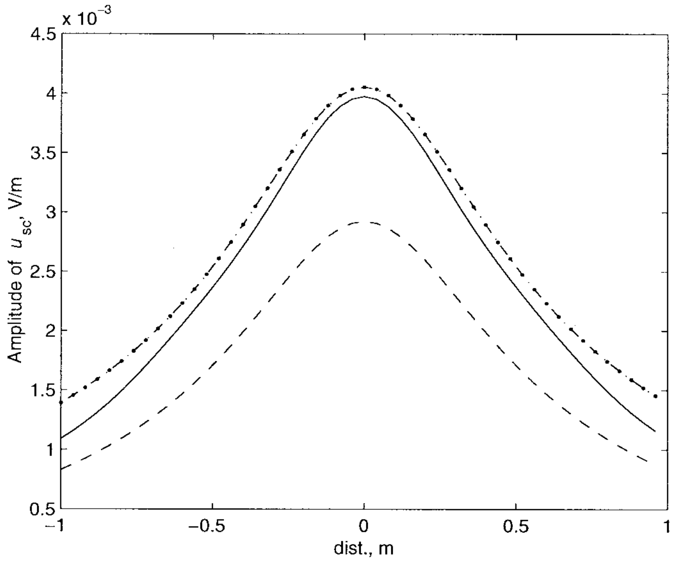

Fig. 3. Test of the approximate forward solution. Amplitude of the scattered field at 100 MHz. Solid line: exact solution; dashed line: single-medium approximation; dashed-and-dotted line: present approximation.

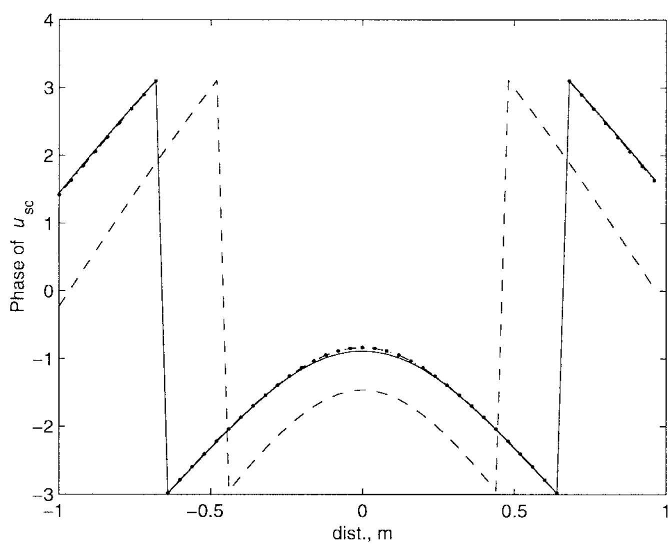

Fig. 4. Test of the approximate forward solution. Phase of the scattered field at 100 MHz. Solid line: exact solution; dashed line: single-medium approximation; dashed-and-dotted line: present approximation.

the lower half space). Figs. 3 and 4 show the amplitude and the phase of the scattered field at 100 MHz for a circular cylinder of the radius $R_c = 0.1$ m, placed 0.2 m below the boundary, with the measurement line situated 0.2 m above the boundary. The distance between source and receiver is set to zero, $R_0 = 0$ m. The permittivity and conductivity of the half space and cylinder are, respectively, $\varepsilon_1/\varepsilon_0 = 3$, $\sigma_1 = 0.01$, and $\varepsilon_c/\varepsilon_0 = 2$, $\sigma_c = 0$. The solid line corresponds to the exact solution, the dashed line stands for the free-space solution with the constitutive parameters of the embedding set to be those of the lower half space, and the dashed-and-dotted line denotes our approximation. This comparison is obviously in favor of the present approximation.

In Figs. 5 and 6, the same configuration is taken, but now the frequency is 500 MHz. The discrepancy in the

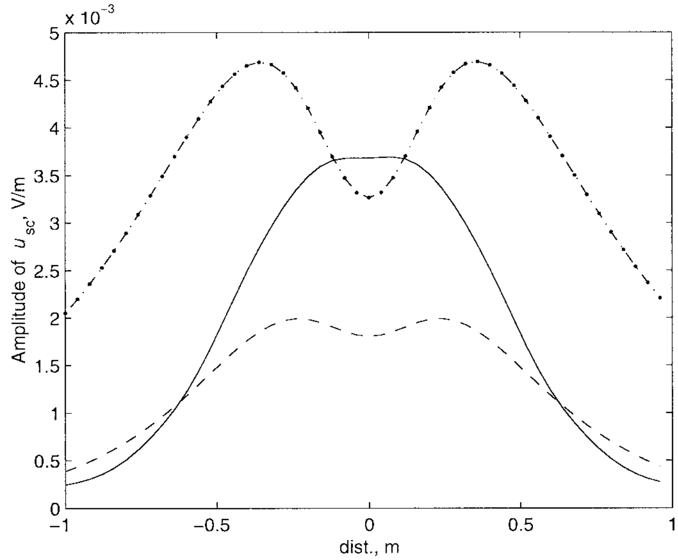

Fig. 5. Test of the approximate forward solution. Amplitude of the scattered field at 500 MHz. Solid line: exact solution; dashed line: single-medium approximation; dashed-and-dotted line: present approximation.

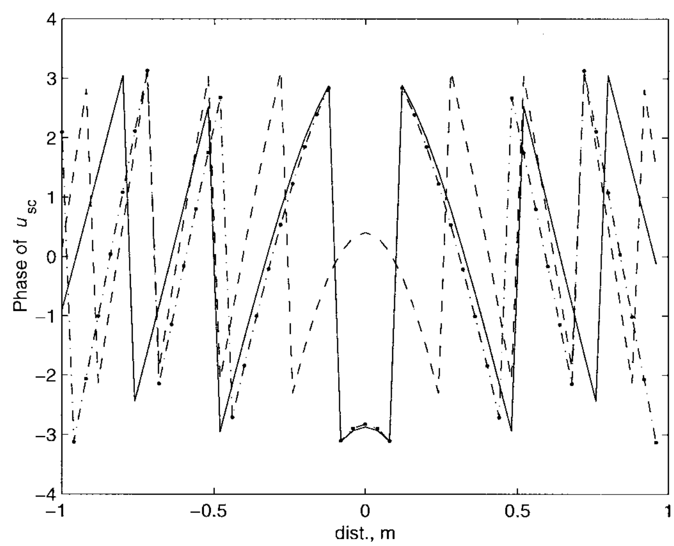

Fig. 6. Test of the approximate forward solution. Phase of the scattered field at 500 MHz. Solid line: exact solution; dashed line: single-medium approximation; dashed-and-dotted line: present approximation.

amplitude is higher, while the phase is still well-approximated by our method in the vicinity of the object. The single-medium approximation is even further from the truth for higher frequencies. The single-medium Green function becomes a reasonable approximation only when the distance between the measurement line and the half-space boundary vanishes, provided the frequency of operation is low enough. However, this case is covered by our approximation as well, which thus appears to be more feasible.

V. Nonlinear Model-Based Inversion

Let us suppose that some arbitrary finite-sized object is present in the lower half space. In the process of inversion, we try to minimize the following nonlinear functional:

$$F^{\mathrm{err}}[x_c, z_c, R_c, \varepsilon_c] = \left\| u^{\mathrm{sct}} - u^{\mathrm{sct}}_{\mathrm{mod}} \right\|. \tag{54}$$

Here, $u^{\mathrm{sct}}_{\mathrm{mod}}$ is the output of our forward solution based on the effective circular scattering model, which is compared to the actual field u^{sct} scattered by the real object. We consider two types of the norm $\|\cdot\|$ in (54). The one defined as

$$\left\|u^{\mathrm{sct}}-u^{\mathrm{sct}}_{\mathrm{mod}}\right\|=\frac{\sum_{\mathbf{r}_r,\mathbf{r}_s,\omega}\left|u^{\mathrm{sct}}-u^{\mathrm{sct}}_{\mathrm{mod}}\right|^2}{\sum_{\mathbf{r}_r,\mathbf{r}_s,\omega}\left|u^{\mathrm{sct}}\right|^2} \tag{55}$$

uses complex amplitudes of the scattered field and therefore demands both amplitude and phase measurements. The other one, defined as

$$\left\|u^{\mathrm{sct}}-u^{\mathrm{sct}}_{\mathrm{mod}}\right\|=\frac{\sum_{\mathbf{r}_r,\mathbf{r}_s,\omega}\left|\left|u^{\mathrm{sct}}\right|-\left|u^{\mathrm{sct}}_{\mathrm{mod}}\right|\right|^2}{\sum_{\mathbf{r}_r,\mathbf{r}_s,\omega}\left|u^{\mathrm{sct}}\right|^2} \tag{56}$$

employs amplitude-only measurements.

No linearization is applied to solve the inverse problem, keeping the functional F^{err} in its original, nonlinear form. The desired (global) minimum of this functional would be the set of parameters, which determines the best approximation of the real object in terms of a simplified circular model. Although we have no guarantee that the global minimum will be obtained, our previous experience from the free-space studies [1] allows us to expect the present algorithm to limit the domain of possible location of the object and provide some knowledge of its material parameters.

VI. Applications of the Algorithm

A difficult problem arises in subsurface sensing if one tries to locate and characterize the object of relatively low dielectric contrast with respect to the background. Such an object produces low anomalous scattered field. Therefore, we concentrate mainly on this situation, which corresponds particularly to the practical problem of location of antipersonnel land mines that are made of polymer materials and that are undetectable with an ordinary land mine detector.

In this section, we consider two different applications of the developed algorithm. The first one concerns the problem of localization of a single spatially compact, buried object using monofrequency scattered data. The second application uses simulated transient GPR response for the characterization of conventional synthetic aperture radar (SAR) images.

A. Localization of Compact Objects Using Monofrequency Data

Here, monofrequency synthetic measurement data are generated using a numerical method based on the domain-integral-equation (CGFFT) method [9]. We study two different inhomogeneous objects having realistic parameters of antipersonnel land mines (plastic, blast-type with low or no metal contents). The permittivity of land mines $\varepsilon_c/\varepsilon_0$ varies between 2.0 and 2.7. The permittivity and conductivity of soil (lower half space) is set to be $\varepsilon_1/\varepsilon_0 = 3$ and $\sigma_1 = 0.01$ Sm. The quasi-Newton method is used for minimization of the error functional (54).

We consider three types of acquisition corresponding to different locations of source and receiver with respect to each other and to the domain containing the object of interest (See Cases A, B, and C of Fig. 7). The first two correspond to the situation in which the object domain is inaccessible by neither source nor receiver. Here, we distinguish the case of source and receiver placed at different sides out of the object domain (stretched bistatic acquisition, Case A), and in which both source and receiver are placed at the same region next to the object domain (shifted monostatic acquisition, Case B). The third acquisition corresponds to the backscattered field measured right above the object domain (local monostatic acquisition, Case C). The total length of the source/receiver path is usually comparable to the size of the object domain. In all of the mentioned acquisitions, the scattered field data are collected in 20 equidistant points of the receiver's path.

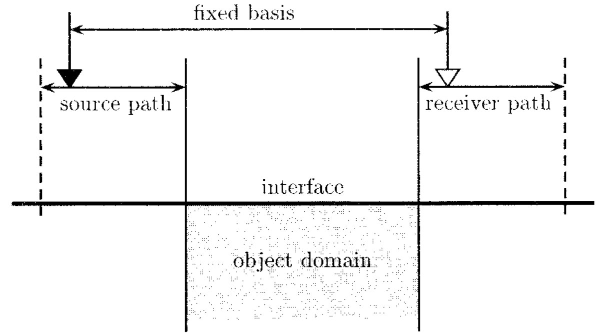

(a)

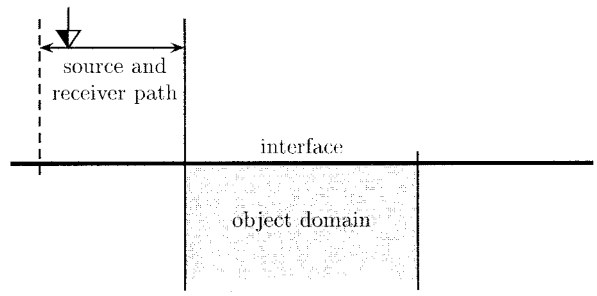

(b)

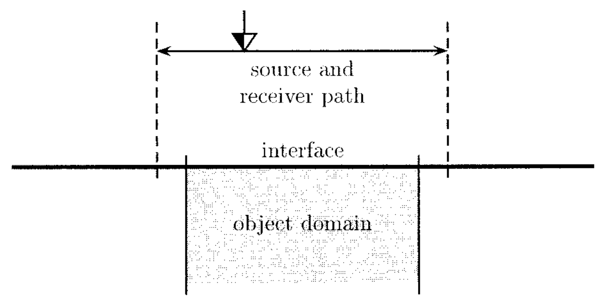

(c)

Fig. 7. Types of acquisition.

Each inversion has been repeated with several different initial guesses to make sure that the obtained result is not occasional. The unknown parameters are subject to the set of natural constraints. From the geometrical point of view, these constraints pose the problem of finding the object whose size is less then 5% of the size of the domain of search (object domain). Although the algorithm has demonstrated very little sensitivity to the choice of initial guess, an initial guess in

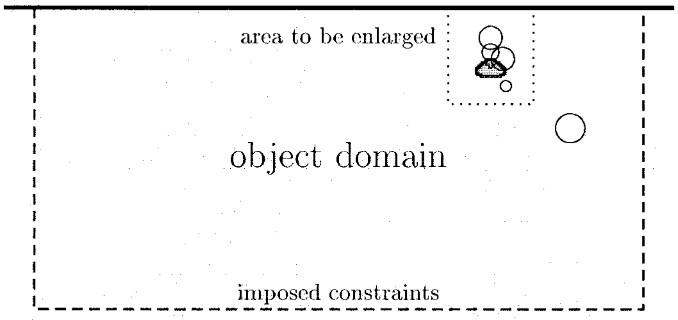

Fig. 8. General view of the object domain with a land mine model (MAI75) in it. Circles represent some of the results of inversion. The dotted rectangular denotes the area to be enlarged in the next figure.

the middle of the imposed constraints provides the fastest convergence.

It is well known that GPR technology is based on frequencies lower then 1 GHz, since an electromagnetic field of higher frequency does not penetrate deep enough into the ground (soil). Normally, the frequency band of GPR starts from 100 MHz. With our method, we propose to invert data obtained at this lowest frequency to get some fast preliminary information about the buried object.

In Figs. 8 and 9, the land mine model (MAI75) is buried at 0.2 m; obviously deeper than in practice. However, this allows us to overview some important features of the algorithm. Fig. 8 gives a general view of the object domain with a land mine model in it and some of the results of location (circles). In the next figure (Fig. 9), the region of Fig. 8 marked with the dotted rectangular is enlarged. Here, the results of inversion using the exact forward solution are presented with solid circumferences, while the dashed ones correspond to the approximation proposed in this paper. We use both amplitude and phase data for the inversion based on the exact code (mainly for reference purposes). The approximation-based code is supplied with amplitude-only scattered data. The inversion process takes substantially different computer time depending upon the type of an underlying forward algorithm. Based on the exact code, it takes more than 1 h. Based on the approximation, it takes less than 1 min (normally, 10–20 s). The type of acquisition is explicitly marked with the corresponding letter (A, B, or C). The distance of the source/receiver path from the interface is set to be 2 m in all the cases, corresponding to the situation where the GPR equipment is mounted on a vehicle.

The acquisition B, which is favorable from the practical point of view (one-side illumination/measurement next to the object domain), presents the worst result with shifts in both vertical and horizontal directions. The scattered data collected in this way do not allow for better inversion. However, keeping in mind that the relative size of the object is 5% of the domain of search in both vertical and horizontal directions (note that comparison of cross sections would give even smaller values), the center of the solid circle gives less then 5% error in each coordinate (acceptable in certain cases). The error for the center of the dashed circle (Case B) is 10–15%. This means that by employing these results, one can reduce the size of the object domain down to 30% of the original in both x and z directions.

When data are collected across the object domain or above it, the horizontal location of the object is almost perfect for the exact code and has an error of less then 5% for the approximation. As can be seen from Fig. 9, the exact code gives the precise location in Case C. The approximation-based inversion remains with some vertical shift, although horizontal location is true.

The radius of the effective circular cylinder tends to be that of the inscribed circle whenever the location of its center is close enough to the true one: solid circle (Case C) and dashed circle (Case A). Note that in the free-space embedding [1], it was a circumscribed circle. To obtain a similar result in subsurface localization, one has to reduce the frequency of operation down from 100 MHz. However, we do not consider this frequency band here, since it is not yet realized in the available compact equipment. Hence, the obtained value of the effective permittivity is less obviously related to that of the volume averaged through the object [it often corresponds to a “stronger” scatterer $(\varepsilon_c/\varepsilon_0 \sim 2)$].

In the next example, a detailed version of which is given in Fig. 10, we consider a somewhat more realistic situation, in which the plastic land mine (FAMA) is buried closer to the surface. The results have been obtained with the approximation-based inversion algorithm. Taking into account the previous results, we apply a two-step procedure. First, the acquisition B is used to reduce the horizontal size of the domain of search. Assuming (quite inductively of course) that the error in the horizontal location is *always* about 15%, we choose the new (reduced) domain to be 30% of the original size, taking the result of location as a center point. At the second stage, we collect new scattered data via the acquisition C right above the new (reduced) object domain and repeat the inversion procedure. The distance from the interface in case B is chosen to be 1.5 m, whereas in case C, we take a lower illumination/measurement path with respect to the interface (0.2 m). The result of the second stage is correct with regard to the center of the object, while the radius of a circle is somewhere in between inscribed and circumscribed ones. The restored effective permittivity corresponds to a “stronger” scatterer $(\varepsilon_c/\varepsilon_0 = 2.1)$.

An attempt has been made to use the *a priori* information about the radius of the cross section and the internal constitution. With these parameters fixed, the two coordinates of the center are left to be determined. The location in this case was much faster. However, the results have the same precision as with all four parameters released. In our previous studies [1], we have tested a similar inversion algorithm with multifrequency data. Opposite to what is expected, the optimization scheme generally does not become more stable, but it will if the frequencies are chosen very carefully. On the other hand, the forward multifrequency code is significantly slower than the one for a single frequency.

From the analysis of the last three figures, one can draw the conclusion that the present method provides a good horizontal location for 2-D objects and determines their inner radius (inscribed circle). The restored permittivity corresponds to that

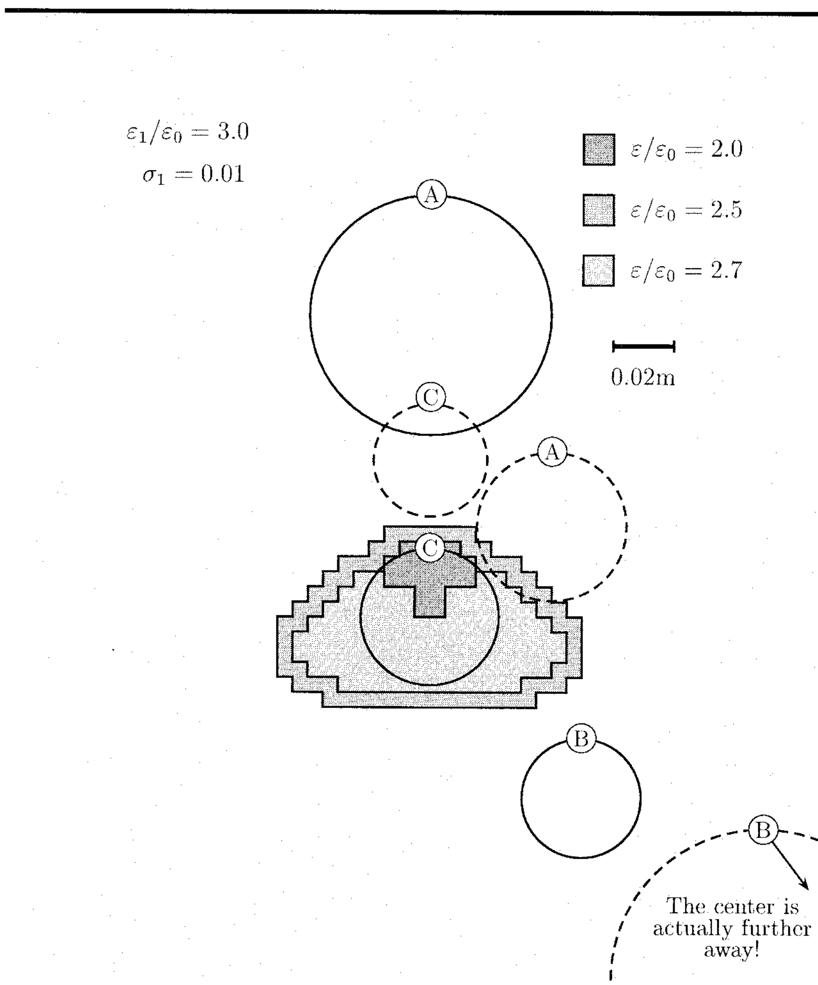

Fig. 9. Localization of a land mine model (MAI75) with different acquisitions (see Fig. 7) and forward codes. Solid circles: exact solution; dashed circles: present approximation.

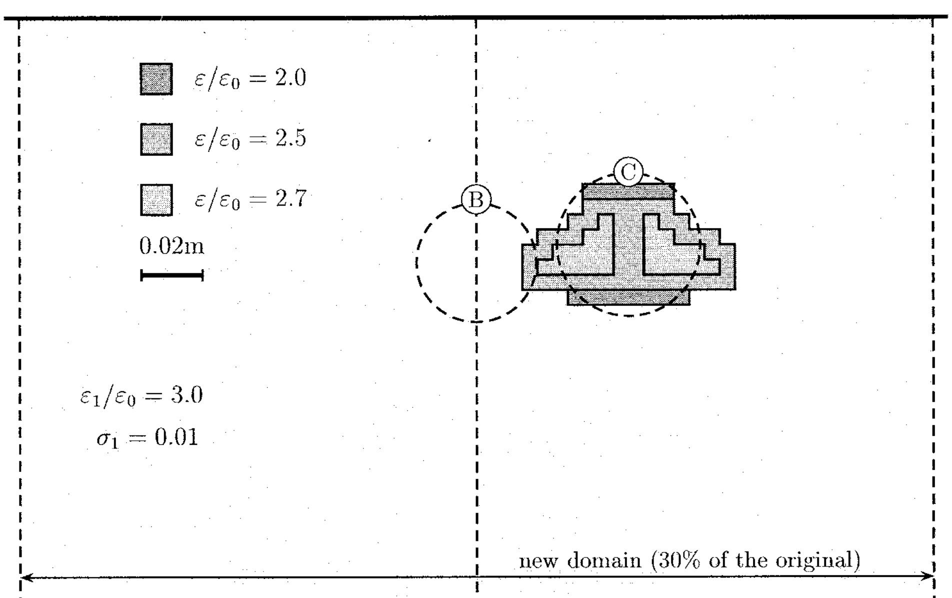

Fig. 10. Two-step localization of a land mine model (FAMA). The acquisition B is used to reduce the horizontal size of the domain down to 30% of the original. Acquisition C then is applied. The approximation-based inversion algorithm has been used with amplitude-only data.

of a stronger scatterer. In terms of the problem of land mine detection, this means that using acquisitions A and B (see Fig. 7), the answer to the question "Where is the land mine buried?" may be quite precise. However, the answer to the question "At what depth is the land mine buried?" will contain a systematic error either due to the lack of measurements (if the exact solution-based code is used) or due to both incomplete data and crude approximation (if the approximation-based code is employed). A solution to this latter problem can be obtained via the two-step inversion procedure described previously.

B. Characterization of SAR Images

In the previous section, we dealt with spatially compact, singled-out, buried objects. However, if there are several scatterers buried close to each other, the localization may run into a wrong local minimum. In order to obtain the information about the location of multiple objects, we perform SAR imaging.

Transient GPR data are generated using the computer code based on the recently developed reduced-order modeling time-domain method [10]. Here, we consider the situation with several objects buried close to the air-soil interface. The set of objects contains two identical plastic land mine models and the model of an igneous mafic weathered rock (see the upper image of Fig. 11). The permittivity of inhomogeneous lossless land mines ranges from 3.0 to 3.5, while the rock has a permittivity of 6.0 and a conductivity of 0.1 Sm. The soil parameters are set to $\varepsilon_1/\varepsilon_0 = 4.0$ and $\sigma_1 = 0.01$. The source-receiver unit of a GPR system corresponds to Acquisition C with the source-receiver offset and the distance from the measurement path to the interface both equal to 0.25 m. The distance between consequent data points is 0.025 m.

The central frequency of the wavelet is approximately 1.6 GHz, although this information and the actual shape of the wavelet are not used in the inversion procedure. We restrict ourselves in this manner, since in practice it is often impossible to obtain such information *a priori*. The time-domain response of the simulated GPR is presented in the second picture of Fig. 11. Here, the vertical axis gives time in nanoseconds, while the horizontal axis corresponds to the position of the midpoint of the source-receiver unit. The effect of the background has been subtracted in this picture (see Step 1).

First we use the simplest SAR technique [11] in order to visualize the contents of the subsurface. In the process of SAR imaging, we employ the homogeneous background model with the permittivity of the medium set to 2.5 (the average between the permittivities of soil and air). As a result, we obtain the image given in the third picture of Fig. 11. Basically, conventional SAR employs the phase of the field, not its amplitude, and thus provides only the *visual* information about the scatterer; its *image*, and is irrelevant to the actual permittivity of the object. At the second stage of this numerical experiment, we propose to use at least some of the amplitude information in order to obtain the effective constitution of subsurface scatterers.

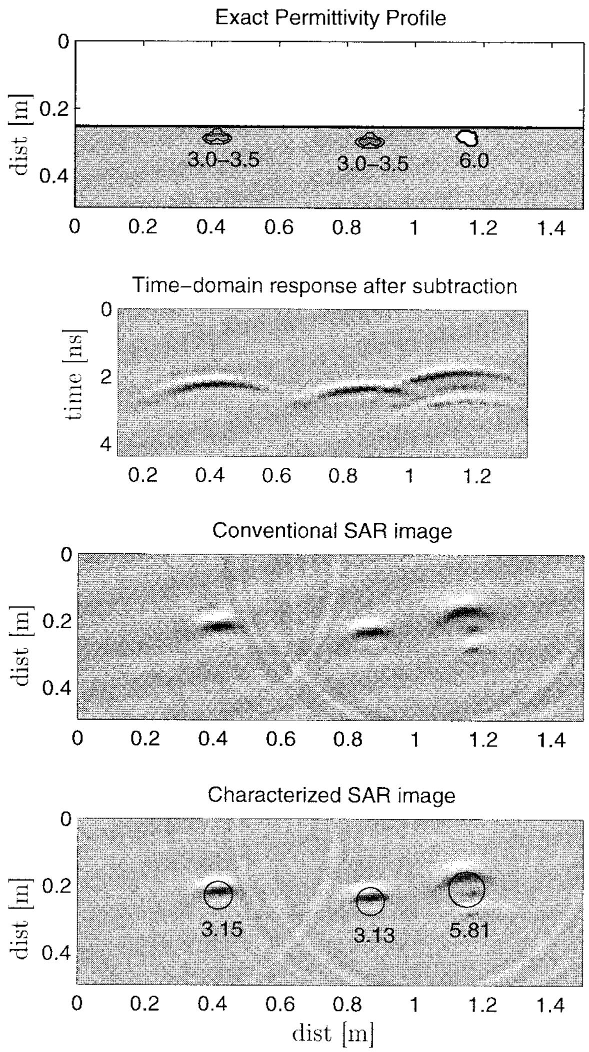

Fig. 11. Characterization of a SAR image. Synthetic time-domain data have been used as an input for the inversion algorithm. Locations and radii are fixed using the visual features of a SAR image.

We select the spatial regions of interest from the SAR image by means of an interactive software. In fact, we circumscribe the parts of the image that could be visually identified as compact scatterers. Having the centers and the radii of the circles fixed, we choose the segments of data which correspond to each particular scatterer. In particular, we have used three sets of five data points each, situated right above the recognizable scatterers in the conventional SAR image.

The method described in the theoretical part of this paper deals with the scattered field due to the monochromatic point source of a unit amplitude, while the time-domain response of a GPR represents the total field in the region due to the wavelet of an unknown shape. Obviously, some preliminary manipulations are needed to adjust and normalize the GPR data.

For the bistatic GPR setup, the data consist of N traces $u(\mathbf{r}_k, t)$, $k = 1, \ldots N$. The incident field in the two-media background $u^{\rm inc}(\mathbf{r}, t)$ can be approximately defined from the trace which corresponds to the part of computational domain without subsurface objects. Let it be the trace with $k = 1$.

Then the incident field in time and frequency domains will be

$$\begin{aligned} u^{\text{inc}}(\mathbf{r},t) &\approx u(\mathbf{r}_1,t), \\ u^{\text{inc}}(\mathbf{r},\omega) &\approx \text{FFT}[u^{\text{inc}}(\mathbf{r},t)]. \end{aligned} \tag{57}$$

Since the field at the receiver has already propagated through the air from the source to the receiver and was reflected by the air–soil interface, we normalize our incident field as follows:

$$u^{\text{inc}}_{\text{NORM}}(\mathbf{r},\omega) \approx \frac{u^{\text{inc}}(\mathbf{r},\omega)}{G_h(\mathbf{r}_r,\mathbf{r}_s,\omega)}. \tag{58}$$

Here, we employ the approximate two-media Green function $G_h(\mathbf{r}_r,\mathbf{r}_s,\omega)$ based on the derivations of this paper.

The scattered transient field at the receiver is obtained by subtracting the incident time-domain field from the rest of the data

$$u^{\text{sct}}(\mathbf{r}_k,t) \approx u(\mathbf{r}_k,t) - u^{\text{inc}}(\mathbf{r},t), \quad k = 1,\ldots N. \tag{59}$$

The normalized frequency-domain counterpart of the scattered field is given by

$$u^{\text{sct}}_{\text{NORM}}(\mathbf{r}_k,\omega) \approx \frac{\text{FFT}[u^{\text{sct}}(\mathbf{r}_k,t)]}{u^{\text{inc}}_{\text{NORM}}(\mathbf{r},\omega)}, \quad k = 1,\ldots N. \tag{60}$$

Finally, after the normalization is complete, we proceed with the optimization for the permittivity of the effective circular scatterers using the corresponding segments of data for each optimization. As it has been explained before, the low-frequency band is the most appropriate for our purposes. We employ the lowest frequency that is still producing a detectable response (270 MHz in our case). The result of this step is given in the fourth (bottom) picture of Fig. 11 with the values of the effective permittivity printed next to the circles. The reconstructed effective permittivities are in good agreement with the exact values. Thus, we have added significant information to the conventional SAR image, which is now not just a simple visualization of the subsurface, but also provides the knowledge of the effective constitution of buried objects.

We would like to add that, although the low-contrast objects were the main concern of this paper, the algorithm has shown essentially the same results with stronger scatterers $(\varepsilon/\varepsilon_0 \leq 20)$. For some high-contrast and large objects, the frequency had to be lowered in accordance with the region of applicability of the introduced approximations.

VII. Conclusion

Two consistent approximations in the forward scattering model have been employed to solve the problem of localization and effective characterization of a 2-D subsurface object from single-frequency, spatially incomplete scattered field data. The first approximation significantly simplifies the two-media Green's function, avoiding numerically expensive spatial inverse Fourier transform. The second approximation, being the essence of the method, models the real object in terms of an effective homogeneous circular scatterer, thus taking into account only the most general features of the scattering process.

Different acquisitions for the GPR system have been studied. If, somehow, neither source nor receiver can be placed close to the surface right above the unknown object, our algorithm still provides a good indication of the place where the object is buried. This result is substantially improved when the scattered data collected in the vicinity of the object are used.

Due to the algorithmic and numerical simplicity of this approach, it can be used in the real-time localization of subsurface objects (land mines, cables, pipes, etc.).

Another important application of the proposed algorithm can be found in the characterization of conventional SAR images. With the help of effective circular scatterers and a fast optimization procedure (10–30 s on a Pentium-type PC), one can obtain valuable information about the effective constitution of subsurface objects.

Our future studies will be concerned with the application of this method to three-dimensional configurations.

Acknowledgment

The authors would like to thank R. Remis of the Delft University of Technology for the time-domain computer code used in the verification of the algorithm presented here.

References

[1] N. V. Budko and P. M. van den Berg, "Two-dimensional object characterization with an effective model," *J. Electromagn. Waves Applicat.*, vol. 12, no. 2, pp. 177–190, 1998.

[2] G. Kristensson and S. Ström, "Scattering from buried inhomogeneities—A general three-dimensional formalism," *J. Acoust. Soc. Amer.*, vol. 64, no. 3, pp. 917–936, 1978.

[3] ——, "Electromagnetic scattering from geophysical targets by means of the T matrix approach: A review of some recent results," *Radio Sci.*, vol. 17, no. 5, pp. 903–912, 1982.

[4] D. O. Batrakov, N. V. Budko, and N. P. Zhuck, "The numerical analysis of the two-dimensional scattering problem for an inclusion in a plane layered medium using the modified null-field method (in Russian)," State Sci.-Tech. Library of Ukraine, Kiev, Ukraine, Tech. Rep 1282-UK95, 1995.

[5] R. E. Kleinman, G. F. Roach, and S. E. G. Ström, "The null field method and modified Green functions," in *Proc. R. Soc. Lond. A*, vol. 394, pp. 121–136, 1984.

[6] B. J. Kooij and M. Lambert, "Nonlinear inversion of a buried object in TE-scattering," in *Proc. IEEE Antennas and Propagation Int. Symp.*, Montreal, Canada, July 13–18, 1997, pp. 2617–2620.

[7] C. Rozier, D. Lesselier, T. S. Angell, and R. E. Kleinman, "Shape retrieval of an obstacle immersed in a shallow water from single-frequency farfields using a complete family method," *Inv. Prob.*, vol. 13, no. 2, pp. 487–508, 1997.

[8] N. K. Uzunoglu and J. D. Kanellopoulos, "Scattering from underground tunnels," *J. Phys. A*, vol. 15, pp. 459–471, Feb. 1982.

[9] A. P. M. Zwamborn and P. M. van den Berg, "The three-dimensional weak form of the conjugate gradient FFT method for solving scattering problems," *IEEE Trans. Antennas Propagat.*, vol. 40, pp. 1757–1767, Sep. 1992.

[10] R. F. Remis and P. M. van den Berg, "A modified Lanczos algorithm for the computation of transient electromagnetic wavefields," *IEEE Trans. Microwave Theory Tech.*, vol. 45, pp. 2139–2149, Dec. 1997.

[11] R. Bamler and P. Hartl, "Synthetic aperture radar interferometry," *Inv. Prob.*, vol. 14, no. 4, pp. R1–R54, 1998.

Neil V. Budko was born in Kharkov, Ukraine, on August 31, 1969. He received the M.Sc. degree in radiophysics in 1992 and the Ph.D. degree in physical and mathematical sciences in 1995, both from the Kharkov State University, Ukraine.

From 1992 to 1995, he was employed by the Chair of Theoretical Radiophysics, Kharkov State University as a Junior Researcher, and in 1995 he was a Senior Researcher and Lecturer. In 1996, he was awarded the Research Fellowship of the Delft University of Technology, Delft, The Netherlands, to conduct research in inverse scattering at the Electromagnetic Research Group. Since 1997, he has been with the same group as a Principal Investigator in a series of externally funded research projects concerned with ground penetrating radar technology. His main research interest is in the physical and mathematical aspects of inverse problems.

Peter M. van den Berg was born in Rotterdam, The Netherlands, on November 11, 1943. He received the degree in electrical engineering from the Polytechnical School of Rotterdam in 1964. He received the B.Sc. and M.Sc. degrees in electrical engineering and the Ph.D. degree in technical sciences, all from the Delft University of Technology, Delft, The Netherlands, in 1966, 1968, and 1971, respectively.

From 1967 to 1968, he was a Research Engineer by the Dutch Patent Office. Since 1968, he has been a member of the Scientific Staff of the Electromagnetic Research Group, Delft University of Technology. During these years, he carried out research and taught classes in the area of wave propagation and scattering problems. During the academic year 1973–1974, he was Visiting Lecturer in the Department of Mathematics, University of Dundee, U.K., financed by an award from the Niels Stensen Stichting, The Netherlands. From 1980 to 1981, he was a Visiting Scientist at the Institute of Theoretical Physics, Goteborg, Sweden. He was appointed as a Professor at the Delft University of Technology in 1981. From 1988 to 1994, he carried out research at the Center of Mathematics of Waves, University of Delaware, Newark. These visits were financed by a NATO award. During the summers of 1993 to 1995, he was a Visiting Scientist at Shell Research B.V., Rijswijk, The Netherlands. Since 1994, he has been a Professor in the Delft Research School Centre of Technical Geoscience. His main research interest is the efficient computation of field problems using iterative techniques based on error minimization, the computation of fields in strongly inhomogeneous media, and the use of wave phenomena in seismic data processing. His other main interest is in an efficient solution to the nonlinear inverse scattering problem.